

Article

The Impact of Numerical Parameters on the Resistance Characteristics of a Container Ship at the Model and Full Scale

Carlo Giorgio Grlj , Nastia Degiuli *  and Ivana Martić 

Faculty of Mechanical Engineering and Naval Architecture, University of Zagreb, Ivana Lučića 5, 10000 Zagreb, Croatia; carlo.g.grlj@fsb.hr (C.G.G.); ivana.martić@fsb.hr (I.M.)

* Correspondence: nastia.degiuli@fsb.hr

Abstract: Computational Fluid Dynamics (CFD) is a powerful tool used to predict the resistance characteristics of a ship. However, it is important to determine the numerical and modelling errors to assure accurate results. The aim of this study is the investigation of the impact of different numerical parameters on the total resistance, wave pattern and ship motion in numerical simulations at the model and full scale. These include the turbulence model and discretization schemes for convection, gradient and temporal terms within the governing equations. The numerical model used in numerical simulations is based on Reynolds Averaged Navier-Stokes (RANS) equations which are discretized using the Finite Volume Method (FVM). To locate and track the free surface, the Volume of Fluid (VOF) method is employed. The Grid Convergence Index (GCI) method is used for the verification study. The obtained results show that the selection of the discretization scheme for temporal term does not have impact on the median value of the total resistance and that the first-order scheme assures faster convergence in numerical simulations at the full scale. A higher portion of the frictional resistance in the total resistance is obtained with numerical simulations at the model scale in comparison to the full scale.

Keywords: CFD; discretization scheme; turbulence model; container ship; resistance test



Citation: Grlj, C.G.; Degiuli, N.; Martić, I. The Impact of Numerical Parameters on the Resistance Characteristics of a Container Ship at the Model and Full Scale. *J. Mar. Sci. Eng.* **2023**, *11*, 1672. <https://doi.org/10.3390/jmse11091672>

Academic Editor: Kostas Belibassakis

Received: 20 July 2023

Revised: 22 August 2023

Accepted: 22 August 2023

Published: 25 August 2023



Copyright: © 2023 by the authors. Licensee MDPI, Basel, Switzerland. This article is an open access article distributed under the terms and conditions of the Creative Commons Attribution (CC BY) license (<https://creativecommons.org/licenses/by/4.0/>).

1. Introduction

Nowadays, Computational Fluid Dynamics (CFD) is a commonly used tool for the prediction of flow around the ship and ship hydrodynamic characteristics, since computational power has been increasing continuously. The main advantage of CFD simulations is that it can reduce the required number of expensive towing tank experiments. Another benefit of the numerical simulations over the towing tank experiments is the possibility of avoiding the extrapolation methods by performing full-scale CFD simulations [1]. Recently, Orych et al. [2] conducted a validation study for the delivered power estimated with numerical simulations based on Reynolds Averaged Navier-Stokes (RANS) equations coupled with a body force propeller method for modelling the effects of a rotating propeller, which is based on the lifting line theory. Numerical uncertainty was determined for numerical simulations at the model and full scale, while the validation was based on sea trial results. The authors obtained an average comparison error between the numerically obtained and sea trial results of about 1%, which is considerably lower than the validation uncertainty equal to 7%. Saydam et al. [3] performed numerical simulations of the resistance, open water and self-propulsion tests for a case of a tanker in order to quantify the numerical simulation uncertainties. The authors found an error of 4% for the prediction of the total resistance, while larger uncertainties were obtained for torque predictions and, consequently, the delivered power.

Degiuli et al. [4] investigated the influence of slow steaming on carbon dioxide (CO₂) emissions by using full-scale CFD simulations based on RANS equations for the determination of resistance and propulsion characteristics. Other aspects, such as the influence

of biofouling on resistance, were studied by Demirel et al. [5]. Song et al. [6] emphasized the importance of including the roughness effects within the CFD simulations for the determination of the frictional and viscous resistance of different hull forms. Feng et al. [7] conducted CFD simulations of a KRISO container ship (KCS) in different water depths for the determination of the total resistance and dynamic sinkage. The numerical results were validated against the benchmark experimental results, and the comparison error was between 1% and 4% with larger errors obtained for the model scale numerical simulations. Full-scale CFD simulations were validated by Niklas and Pruszek [8], and the obtained relative deviation of total resistance in calm water was from -10% to 4% compared to the sea trial data and extrapolated towing tank results. The authors emphasized the importance of determining the form factor, which can vary depending on the method used, and thus, it can have a great influence on the ship resistance predictions. Terziev et al. [1] used CFD simulations to investigate the influence of ship speed and scale on the form factor and concluded that it depends on the Froude number for very low ship speeds, while larger differences in the form factor were obtained for different scales and turbulence models. Dogrul [9] pointed out scale effects on the propulsion characteristics, such as nominal wake, thrust deduction fraction, and open-water propeller and propulsion efficiencies for the case of a Joubert BB2 submarine.

Although full-scale CFD simulations may be a good alternative to towing tank tests, since the extrapolation of the measured values is avoided, there is still a need for a more systematic and comprehensive sea trials in order to validate the numerical simulations at the full scale for the determination of the ship resistance characteristics and the nominal wake [10]. In addition, there is a need to investigate the influence of numerical parameters such as the discretization schemes for solving the convection, gradient and temporal terms within the governing equations. Such a study was conducted by Andrun et al. [11], where the authors assessed the effect of different schemes for solving the gradient terms within the Volume of Fluid (VOF) method by conducting numerical simulations of the flow around the model of the Wigley hull. It was concluded that second-order schemes have to be used on realistic hull forms, for which the non-linear effects are more pronounced, to determine the resistance and wave elevation more accurately. A more recent study was conducted by Huang et al. [12], in order to determine the ideal numerical setup for full-scale numerical simulations. The authors showed that the second-order scheme should be used for spatial discretization, while for temporal discretization, either first or second-order schemes can be applied. The effect of different draughts on the hydrodynamic characteristics was investigated by Farkas et al. [13]. Based on the obtained results, the authors concluded that although RSM turbulence model is the most accurate one, by using the Realizable $k - \epsilon$ (RKE), satisfactory agreement with the extrapolated towing tank results can be obtained. Degiuli et al. [14] numerically investigated the impact of the bulbous bow on the total resistance of a yacht and validated the results by comparing them with the towing tank results. Within the study, the authors achieved satisfactory agreement with the experimentally obtained values for total resistance using different turbulence models.

In this study, numerical simulations of viscous flow around the hull of a container ship are systematically performed in order to assess the effects of different discretization schemes and turbulence models on the hydrodynamic performance in calm water. The effect of numerical parameters are investigated at the model and full scale. The post-Panamax 6750-TEU container ship is chosen since the geometry and inertial properties are available in the literature [15]. An extensive verification study for grid size and time step is performed using the Grid Convergence Index (GCI) method. For numerical simulations at the model scale, a validation study is conducted by comparing the numerical results against the measured values from towing tank tests. The paper is organized as follows. The description of the container ship used in the numerical simulations is provided in Section 2. The mathematical background, the numerical setup and an overview of the verification and validation studies are given in Section 3. The results are discussed in Section 4, and

finally, the conclusions drawn from the comprehensive numerical study are summarized in Section 5.

2. Case Study

The post-Panamax 6750-TEU container ship is selected as a case study. Table 1 shows the geometrical and inertial properties of the model in scale ($\lambda = 35.18$) and full-scale container ship [15], while Figure 1 shows the 3D model used in the simulations.

Table 1. Post-Panamax 6750-TEU container ship data.

Property	Full Scale	Model Scale
λ , -	1	35.18
L_{OA} , m	300.891	8.553
L_{PP} , m	286.6	8.147
L_{WL} , m	281.3	7.996
T , m	11.98	0.341
B , m	40	1.137
Δ , t	85,562.7	1.965
KM , m	18.662	0.531
GM , m	2.1	0.06
KG , m	16.562	0.471
L_{CG} from AP, m	138.395	3.934
k_{xx} , m		14.6
k_{yy} , m		70.144
k_{zz} , m		70.144

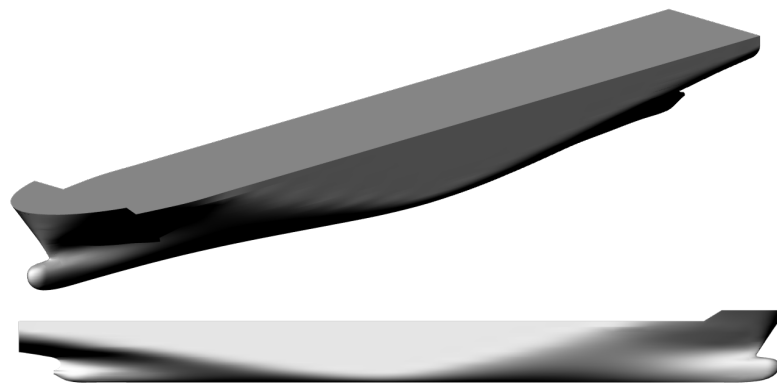


Figure 1. Geometry of the post-Panamax 6750-TEU container ship.

The towing tank experiments were conducted at the Brodarski Institute in Zagreb [16]. The resistance tests were carried out in a large towing tank of a length of 276 m, a width of 12.5 m, and a depth of 6 m. The ship model was made of wood at a scale of $\lambda = 35.18$. The resistance tests were conducted at 14 speeds in the range from 12 to 25 knots corresponding to full-scale ship. For purpose of the validation study, the experimental results of the resistance test at 2.168 m/s are used, corresponding to 25 knots for the full-scale ship.

3. Methods

In this study, numerical simulations based on RANS equations are conducted. The Finite Volume Method (FVM) is used for the discretization of the governing equations. A multiphase flow model based on the Eulerian approach; i.e., the VOF method is used for locating and tracking the free surface. To maintain a sharp interface between two fluids, High-Resolution Interface Capturing (HRIC) scheme is used. The Dynamic Fluid Body Interaction (DFBI) model with two degrees of freedom is used to predict the trim and sinkage.

3.1. Mathematical Model

The commercial software package STAR-CCM+ [17] is used in this study. The mathematical model is based on the RANS equations, which are derived from the conservation of mass and momentum laws. For incompressible, unsteady case the RANS equations read as follows:

$$\frac{\partial \bar{u}_i}{\partial x_i} = 0 \tag{1}$$

$$\rho \frac{\partial \bar{u}_i}{\partial t} + \rho \frac{\partial}{\partial x_j} (\bar{u}_i \bar{u}_j + \overline{u'_i u'_j}) = -\frac{\partial \bar{p}}{\partial x_i} + \bar{\tau}_{ij} \tag{2}$$

where ρ is the fluid density, \bar{u}_i is the averaged Cartesian components of the velocity vector, $\overline{\rho u'_i u'_j}$ is the Reynolds Stress Tensor (RST), and \bar{p} is the mean pressure. The mean viscous stress tensor $\bar{\tau}_{ij}$ is defined by:

$$\bar{\tau}_{ij} = \mu \left(\frac{\partial \bar{u}_i}{\partial x_j} + \frac{\partial \bar{u}_j}{\partial x_i} \right) \tag{3}$$

where μ is the dynamic viscosity of the fluid. The turbulence models are then used to close the system of Equations (1) and (2) to be able to solve them.

3.2. Turbulence Models

Three turbulence models are used in this study: RKE, Shear Stress Transport $k - \omega$ (SSTKO) and RSM. The RANS turbulence models are based on the modelling of the RST. The RKE and SSTKO turbulence models belong to the group of eddy viscosity models, which are based on the similarity between the molecular gradient-diffusion process and turbulent motion. These types of turbulence models use the Boussinesq approximation to model the RST as follows:

$$-\overline{\rho u'_i u'_j} = \mu_t \left(\frac{\partial \bar{u}_i}{\partial x_j} + \frac{\partial \bar{u}_j}{\partial x_i} \right) - \frac{2}{3} \rho k \delta_{ij} \tag{4}$$

where μ_t is the turbulent eddy viscosity, and k is the turbulence kinetic energy.

The RSM turbulence model calculates the components of the RST directly. Thus, it has the potential to predict complex turbulent fluid flows more accurately by considering the anisotropy of the RST, but at the cost of more computational power. More details regarding the applied turbulence models can be found in the literature [13].

3.3. Realizable $k - \epsilon$ (RKE) Two-Layer

The Realizable $k - \epsilon$ Two-Layer turbulence model solves one equation for the turbulent kinetic energy k and one for the turbulent dissipation rate ϵ . The eddy viscosity is calculated as follows:

$$\mu_t = \rho C_\mu \frac{k^2}{\epsilon} \tag{5}$$

where C_μ is the model coefficient defined with the following equation:

$$C_\mu = \frac{1}{A_0 + A_S U^* \frac{k}{\epsilon}} \tag{6}$$

where $A_0 = 4$ and A_S is given by:

$$A_S = \sqrt{6} \cos \phi \tag{7}$$

$$\phi = \frac{1}{3} \arccos(\sqrt{6}W) \tag{8}$$

$$W = \frac{S_{ij}S_{jk}S_{ki}}{(\sqrt{S_{ij}S_{ij}})^3} \tag{9}$$

and U^* is defined as:

$$U^* = \sqrt{S_{ij} \cdot S_{ij} + W_{ij} \cdot W_{ij}} \tag{10}$$

The strain rate tensor is given by the equation:

$$S_{ij} = \frac{1}{2} \left(\frac{\partial u_i}{\partial x_j} + \frac{\partial u_j}{\partial x_i} \right) \tag{11}$$

and the rotation rate tensor by:

$$W_{ij} = \frac{1}{2} \left(\frac{\partial u_i}{\partial x_j} - \frac{\partial u_j}{\partial x_i} \right) \tag{12}$$

The transport equations for k and ε are defined as:

$$\begin{aligned} \frac{\partial}{\partial t}(\rho k) + \frac{\partial}{\partial x_i}(\rho k \bar{u}_i) = & \frac{\partial^2 k}{\partial x_i^2} \left(\mu + \frac{\mu_t}{\sigma_k} \right) + f_c G_k + G_b - Y_M - \\ & - \rho(\varepsilon - \varepsilon_0) + S_k \end{aligned} \tag{13}$$

$$\begin{aligned} \frac{\partial}{\partial t}(\rho \varepsilon) + \frac{\partial}{\partial x_i}(\rho \varepsilon \bar{u}_i) = & \frac{\partial^2 \varepsilon}{\partial x_i^2} \left(\mu + \frac{\mu_t}{\sigma_\varepsilon} \right) + \frac{1}{T_\varepsilon} C_{\varepsilon 1} (f_c S k + C_{\varepsilon 3} G_b) - \\ & - C_{\varepsilon 2} f_2 \rho \left(\frac{\varepsilon}{T_\varepsilon} - \frac{\varepsilon_0}{T_0} \right) + S_\varepsilon \end{aligned} \tag{14}$$

where \bar{u}_i is the averaged velocity vector, σ_k and σ_ε are the turbulent Schmidt numbers, f_c is the curvature correction factor, G_k is the turbulent production term, G_b is the buoyancy production term, ε_0 is the ambient turbulence value that counteracts turbulence decay, Y_M is the dilatation dissipation, $C_{\varepsilon 1}$, $C_{\varepsilon 2}$ and $C_{\varepsilon 3}$ are the model depending coefficients, S_k and S_ε are the user-defined source terms, and S is the modulus of the mean strain tensor.

3.4. Shear Stress Transport $k - \omega$ (SSTKO)

The $k - \omega$ turbulence model is a two-equation model that solves transport equations for the turbulent kinetic energy k and another for the specific dissipation ω :

$$\begin{aligned} \frac{\partial}{\partial t}(\rho k) + \frac{\partial}{\partial x_i}(\rho k \bar{u}_i) = & \frac{\partial^2 k}{\partial x_i^2} (\mu + \sigma_k \mu_t) + G_k + G_{nl} + G_b - \\ & - \rho \beta^* f_{\beta^*} (\omega k - \omega_0 k_0) + S_k \end{aligned} \tag{15}$$

$$\frac{\partial}{\partial t}(\rho \omega) + \frac{\partial}{\partial x_i}(\rho \omega \bar{u}_i) = \frac{\partial^2 \omega}{\partial x_i^2} (\mu + \sigma_\omega \mu_t) + G_\omega + D_\omega - \rho \beta f_\beta (\omega^2 - \omega_0^2) + S_\omega \tag{16}$$

where σ_k , σ_ω , β and β^* are the model depending coefficients, G_{nl} is the non-linear production term, f_β is the free-shear modification factor, f_{β^*} is the vortex-stretching modification factor, and finally, k_0 and ω_0 are the ambient values that counteract turbulence decay. Menter [18] modified the Standard $k - \omega$ model, which blends the $k - \varepsilon$ model in the

far-field with the $k - \omega$ model near the wall. The turbulent eddy viscosity is given with the following equation:

$$\mu_t = \rho k T \tag{17}$$

where T is the turbulent time scale given with the equation:

$$T = \min\left(\frac{\alpha^*}{\omega}, \frac{a_1}{SF_2}\right) \tag{18}$$

where α^* and a_1 are the model coefficients, and F_2 is the blending function coefficient that depends on the distance to the wall.

3.5. Reynolds Stress Model (RSM)

The Reynolds Stress Model consists of solving the transport equation for RST. The transport equation is defined as:

$$\begin{aligned} \frac{\partial}{\partial t}(\rho R_{ij}) + \frac{\partial}{\partial x_i}(\rho R_{ij} \bar{u}_i) = & \frac{\partial}{\partial x_m} \left[\left(\mu + \frac{\mu_t}{\sigma_k} \right) \frac{\partial R_{ij}}{\partial x_m} \right] + P_{ij} + G_{ij} - \\ & - \frac{2}{3} Y_M + \phi_{ij} - \rho \varepsilon_{ij} + S_R \end{aligned} \tag{19}$$

where P_{ij} is the turbulent production term, G_{ij} is the buoyancy production term, ϕ_{ij} is the pressure-strain tensor, and ε_{ij} is the turbulent dissipation rate tensor. This model requires seven equations to be solved, six equations for the RST components and one equation for the isotropic turbulent dissipation. The Quadratic Pressure-Strain model was used within the simulations with high y^+ wall treatment to model the pressure-strain term.

3.6. Computational Domain and Boundary Conditions

An unstructured hexahedral mesh is used for the discretization of the computational domain. Only half of the computational domain is created, since the flow is symmetric with respect to the ship symmetry plane. The domain boundaries are placed at a distance to avoid their influence on the flow around the ship hull and consequently on the obtained results. The inlet and bottom boundaries are placed at $2L_{PP}$ from the ship, the top boundary is placed at L_{PP} above the waterline, while the outlet boundary is placed at $4L_{PP}$ behind the ship. The side boundary is placed at $2.5L_{PP}$ to avoid reflection of the waves. Boundary conditions are set as the VOF wave velocity at the inlet, top and bottom boundaries. The pressure outlet is assigned at the outlet boundary, while both sides of the domain are defined as symmetry planes. The no-slip wall boundary condition is set at the hull surface. The computational domain with the respective boundary conditions and its main dimensions is given in Figure 2. In order to prevent wave reflection against the domain boundaries, the wave damping layer approach is used in the numerical simulations. The wave damping is applied at the inlet, outlet and side boundaries.

Different regions around the ship are carefully discretized. The grid is more refined in the area where the free surface is expected to be located as well as the Kelvin wake region behind the ship, following the ITTC recommendations [19]. The region close to the ship hull is refined with more attention given to the bow and stern regions.

The prism layers are carefully generated so that the non-dimensional wall distance y^+ is in the range $30 < y^+ < 100$, i.e., the log-law region [20]. The approximate distance between the wall and the centre of the first prism layer near the wall is calculated as:

$$y = \frac{y^+ L}{0.172 Re^{0.9}} \tag{20}$$

where Re is the Reynolds number. The obtained non-dimensional wall distance y^+ is within the limits, as shown in Figure 3, meaning that the application of wall functions is justified. Figure 4 shows the fine grid with the described refinements, which is used

within the numerical simulations. Figure 5 shows a detailed view of the stern and bow regions. It can be noticed that the prism layers are carefully created to obtain a smooth transition between the prism layers and the rest of the grid. The stretching factor for the prism layers is about 1.5, and the number of prism layers depends on the scale for which the numerical simulations are conducted. A lower number of prism layers are created at the model scale and a higher number at the full scale to achieve a prism layer thickness that assures a smooth transition from prism layers to the rest of the grid. The prism layers are not generated on the deck and transom stern surfaces.

The distributions of the pressure coefficients along the hull surface obtained from numerical simulations at the model and full scale are shown in Figure 6. Lower pressure coefficients are achieved in the bulbous bow region for the model scale in comparison to full scale.

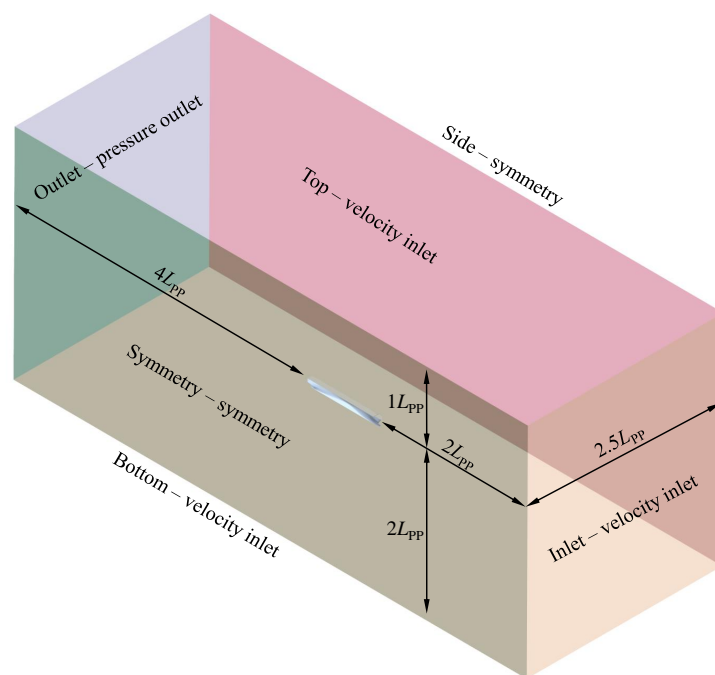


Figure 2. Dimensions and boundaries of the computational domain for the free surface simulations.

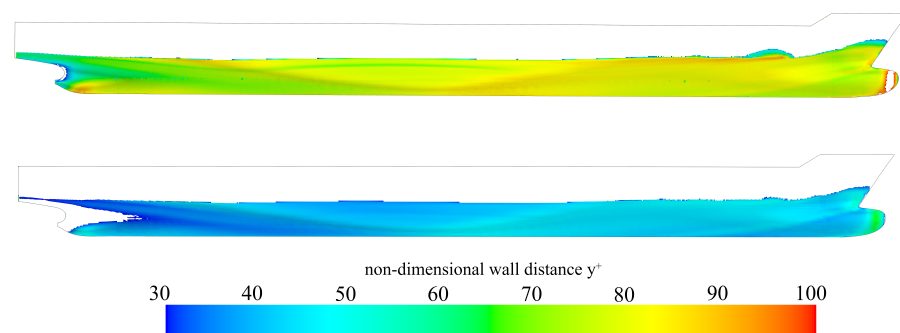


Figure 3. Distribution of the non-dimensional wall distance y^+ on the full scale (top) and model scale (bottom) hull surface.

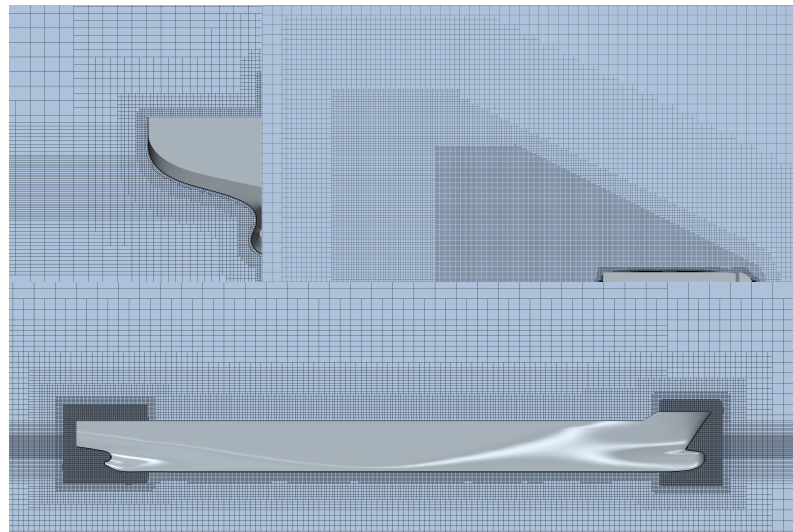


Figure 4. Fine grid with refinements.

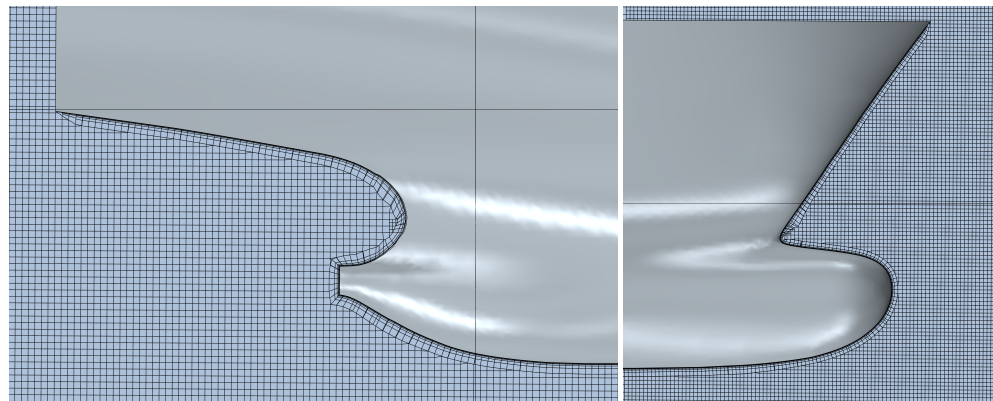


Figure 5. Detailed view of the prism layers at the stern (left) and bow (right).

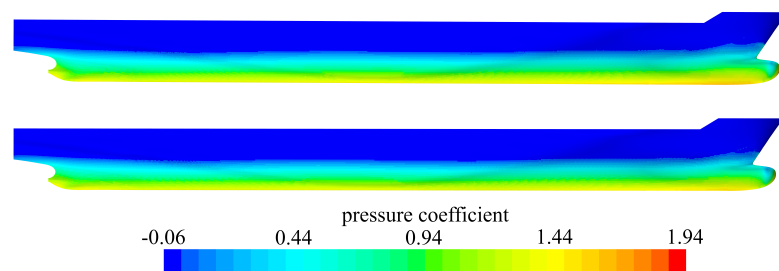


Figure 6. Distribution of the pressure coefficient on the hull surface at full scale (top) and model scale (bottom).

In the numerical simulations, a speed of 25 knots corresponding to the full-scale ship is used. Froude similarity is used to calculate the speed for the numerical simulations at the model scale.

3.7. The Verification And Validation Study

The GCI method is used for the verification study, which is based on the Richardson extrapolation [21]. This method was successfully used in [20,22,23]. The first step is to calculate the apparent order of the method p using the following equations:

$$p = \frac{1}{\ln r_{21}} \cdot \left| \ln \left| \frac{\epsilon_{32}}{\epsilon_{21}} \right| + q(p) \right| \quad (21)$$

$$q(p) = \ln\left(\frac{r_{21}^p - s}{r_{32}^p - s}\right) \tag{22}$$

$$s = 1 \cdot \operatorname{sgn}\left(\frac{\varepsilon_{32}}{\varepsilon_{21}}\right) \tag{23}$$

where r is the grid refinement ratio, and ε is defined as $\varepsilon_{ij} = \phi_i - \phi_j$, with ϕ being the solutions. The order of the method p is calculated by solving the Equations (21)–(23) iteratively.

Extrapolated values and the approximate and extrapolated relative errors are calculated using the Equations (24)–(26), respectively:

$$\phi_{\text{ext}}^{21} = \frac{r_{21}^p \phi_1 - \phi_2}{r_{21}^p - 1} \tag{24}$$

$$e_a^{21} = \left| \frac{\phi_1 - \phi_2}{\phi_1} \right| \tag{25}$$

$$e_{\text{ext}}^{21} = \left| \frac{\phi_{\text{ext}}^{21} - \phi_1}{\phi_{\text{ext}}^{21}} \right| \tag{26}$$

Finally, GCI for fine grid can be calculated with following equation:

$$GCI_{\text{fine}}^{21} = \frac{1.25e_a^{21}}{r_{21}^p - 1} \tag{27}$$

The convergence condition R is calculated with the following equation:

$$R = \frac{\varepsilon_{21}}{\varepsilon_{32}} \tag{28}$$

Convergence conditions R are used to evaluate the obtained extrapolated values and are defined as:

- Monotonic convergence: $0 < R < 1$;
- Oscillatory convergence: $R < 0$;
- Divergence: $R > 1$.

The described method can be used for the calculation of the uncertainty due to time step [24]. Fine grid is used, and three time steps are varied in the numerical simulations for the determination of the uncertainty due to time step.

3.8. Discretization Schemes

The RANS equations are discretized in order to be able to numerically solve them. More precisely, the governing Partial Differential Equations (PDE) are transformed into a system of algebraic equations. In this study, different discretization schemes for spatial and temporal discretization are used, and the obtained results are compared. Specifically, the convection terms are solved using three discretization schemes, while the gradient and temporal terms are solved using two discretization schemes.

The convection terms in the segregated flow and turbulence models can be solved using different schemes within the software package STAR-CCM+. The second-order scheme is used for the verification and validation study. Thereafter, first- and third-order schemes are investigated. The results obtained by the first and second-order discretization schemes for gradient terms are then compared. Finally, the investigated parameters, i.e., discretization schemes for gradient, convection terms and temporal discretization are all set as first and second order. An overview of the different combinations used in numerical simulations can be found in Section 4.

4. Results and Discussion

4.1. The Verification and Validation Study

The verification study is performed for time step and grid size at the model and full scale. Time steps are selected according to the ITTC recommendations [19] in the range $0.005L_{WL}/v - 0.01L_{WL}/v$. The largest time step used in this study is $0.02L_{WL}/v$, and hence, the refinement ratio is equal to 2, and consequently, the iterative procedure for obtaining the order of the method p is avoided.

The details of the used grid resolutions are presented in Table 2. The grid spacing value h is defined as:

$$h = \sqrt[3]{\frac{1}{N} \sum_{i=1}^N (\Delta V_i)} \tag{29}$$

where N is the total number of cells in the grid, and V_i is the volume of the i -th cell.

Table 2. Details of the used grid resolutions.

Index	N		h, m	
	Model Scale	Full Scale	Model Scale	Full Scale
1	2.3 M	3.7 M	0.189	7.70
2	1.0 M	2.3 M	0.248	8.99
3	0.4 M	1.0 M	0.327	11.99

Tables 3 and 4 show all the calculated variables and the estimation of errors for two verification studies at the model and full scales. The approximated and extrapolated relative errors are presented alongside the GCI. Monotonic convergence is obtained for the full-scale numerical simulations and oscillatory convergence for both verification studies at the model scale. The obtained numerical uncertainty is below 2% for all cases, which shows that the fine grid size and time step are adequate for the remaining numerical simulations. It is worth noting that the obtained GCI for full-scale numerical simulations is slightly higher in comparison to model scale numerical simulations. One of the reasons is the grid setup within the numerical simulations.

Table 3. Verification study for the time step.

Parameter	Model Scale	Full Scale
ϵ_{32}	−7.906 N	80.524 kN
ϵ_{21}	1.259 N	31.774 kN
r_{32}	2	2
r_{21}	2	2
R	−0.159	0.395
p	2.650	1.342
e_a^{21}	0.014%	0.01%
e_{ext}^{21}	0.003%	0.01%
GCI_{fine}^{21}	0.34%	1.13%

Table 4. Verification study for the grid size.

Parameter	Model Scale	Full Scale
ϵ_{32}	1.897 N	80.756 kN
ϵ_{21}	−0.013 N	9.885 kN

Table 4. Cont.

Parameter	Model Scale	Full Scale
r_{32}	1.319	1.335
r_{21}	1.314	1.167
R	−0.006	0.123
p	18.142	6.228
e_a^{21}	0.0001%	0.44%
e_{ext}^{21}	0.000001%	0.27%
GCJ_{fine}^{21}	0.0001%	0.34%

The obtained numerical results for the model scale are validated against the measured values obtained by the towing tank tests. To compare the numerical and experimental results, the relative deviation is calculated as follows:

$$RD = \frac{\phi_{CFD} - \phi_{EXP}}{\phi_{EXP}} \cdot 100\% \tag{30}$$

where ϕ_{CFD} and ϕ_{EXP} are numerically and the experimentally obtained values, respectively. Table 5 shows the numerically and experimentally obtained total resistance and the calculated relative deviations for the speed of 25 knots and three turbulence models. It can be seen that the relative deviations are quite high, but that is in accordance with a previous study conducted by Farkas et al. [13], where the highest relative deviations are obtained using the SSTKO turbulence model. Similar results were shown in a review paper by Pena and Huang [25], where the authors showed that relative deviations of 10% can be expected with eddy viscosity turbulence models when wall functions are applied. It is important to note that the numerical simulations are performed for a smooth hull surface, so underprediction of the total resistance is expected. Thus, although the RKE turbulence model shows the lowest relative deviation, it overpredicts the total resistance. In conclusion, the SSTKO turbulence model is selected since it is the best compromise between the computational time and the accuracy of the results.

Table 5. Validation study for the total resistance.

Turbulence Model	$R_{TM,CFD}$, N	$R_{TM,EPD}$, N	RD, %
RKE	96.617		1.709
SSTKO	87.780	94.994	−7.595
RSM	91.352		−3.834

4.2. Turbulence Models

In Section 4.2, the SSTKO turbulence model is compared to the RKE and RSM models. The numerical simulations with the SSTKO turbulence model were conducted until the total resistance converged. After the stable oscillations of the total resistance were reached, the simulations were performed for an additional 200 s for the full scale and around 100 s for the model scale. The medians of these oscillations are calculated, and the obtained total resistances are shown in Table 6.

Table 6. Total resistance obtained with RKE, SSTKO and RSM turbulence model.

Turbulence Model	R_{TS} , kN	R_{TM} , N
RKE	2321.11	96.62
SSTKO	2302.87	87.73
RSM	2356.26	91.35

Figure 7 shows the values of the total resistance as a function of physical time for three turbulence models. The oscillations are caused partly by the trim and sinkage of

the ship. The total resistance obtained with the SSTKO turbulence model at the full scale is slightly lower than for RSM and RKE models, which predict similar results. From Table 6 and Figure 7 it can be seen that the RSM turbulence model yields the highest total resistance at the full scale. Also, the trend of the total resistance curve is almost the same for all three turbulence models. It should be noted that the median values of total resistance obtained by all turbulence models are similar. At the model scale, the trend of the total resistance curve varies significantly with the turbulence model, where the RKE predicts significantly higher values in comparison to the SSTKO and RSM turbulence models. One of the reasons for this is that the numerical setups are different regarding the discretization of the boundary layer, with less prism layers generated at the model scale when compared to the full scale. The reason for the higher values obtained with the RKE turbulence model is that the eddy viscosity is calculated differently than when using the SSTKO turbulence model. This effect is visible at the model scale since the boundary layer is relatively larger when compared to the full scale.

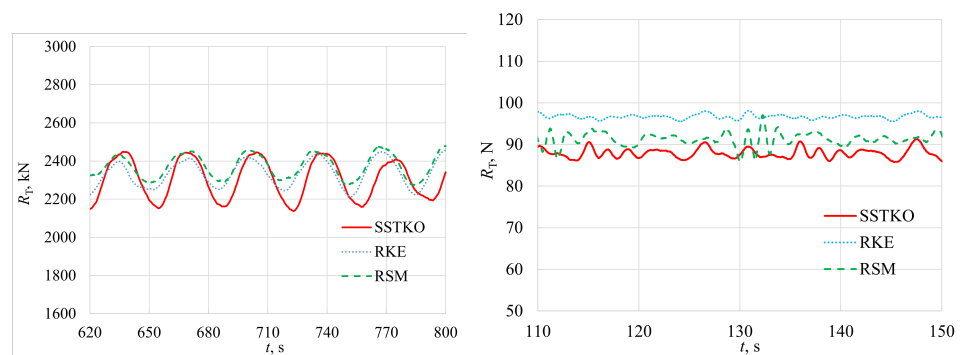


Figure 7. Comparison of total resistance obtained using three turbulence models at full scale (left) and model scale (right).

Figure 8 shows the sinkage and trim as a function of the physical time at the full scale and model scale. The sinkage obtained with numerical simulations at the model scale is scaled with $\lambda = 35.18$ for the comparison with full-scale results. It can be seen that trim does not depend on the chosen turbulence model at the full scale, while sinkage is slightly lower for the RSM turbulence model. At the model scale, the RSM turbulence model predicts lower sinkage and higher trim values. The sinkage and trim obtained with the RKE and SSTKO turbulence model are nearly the same at the full and model scale. The sinkage and trim obtained using the RSM turbulence model at the model scale are similar to the results at the full scale. However, the trim is lower and sinkage is higher when using the SSTKO and RKE turbulence models at the model scale in comparison to the full scale.

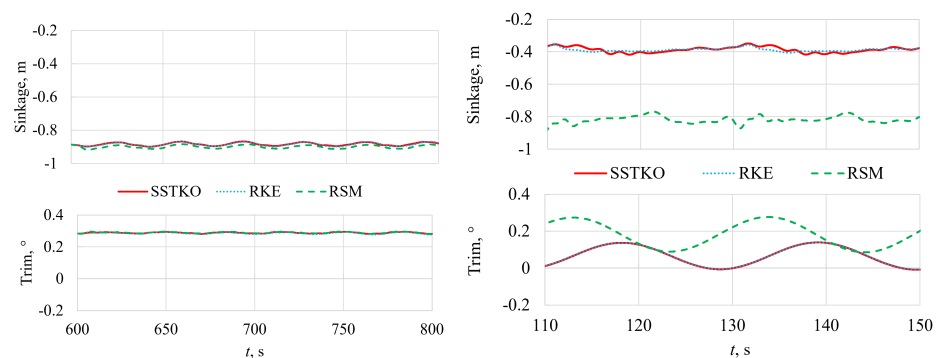


Figure 8. Sinkage and trim values as a function of physical time for three turbulence models at full scale (left) and model scale (right).

Figure 9 shows the wave elevations along the hull and Figure 10 on the longitudinal cuts located at $B/4$, $B/2$ and B from the centreline of the ship, obtained with different turbulence models at the model and full scale. The wave elevations are presented in the non-dimensional form by dividing the x -axis and wave elevations η with length between perpendiculars L_{PP} . The differences between turbulence models are not significant, although at both scales, there are some discrepancies near the bow. At the full scale, the RSM and SSTKO turbulence model predict similar wave elevations, while the RKE yields slightly different results. Also, at the full scale, the RKE turbulence model predicts a higher wave elevation at longitudinal distance between $0.2L_{PP}$ and $0.3L_{PP}$. Similar results are obtained using the RSM and RKE turbulence model at the model scale but with lower values near the bow in comparison to the full scale.

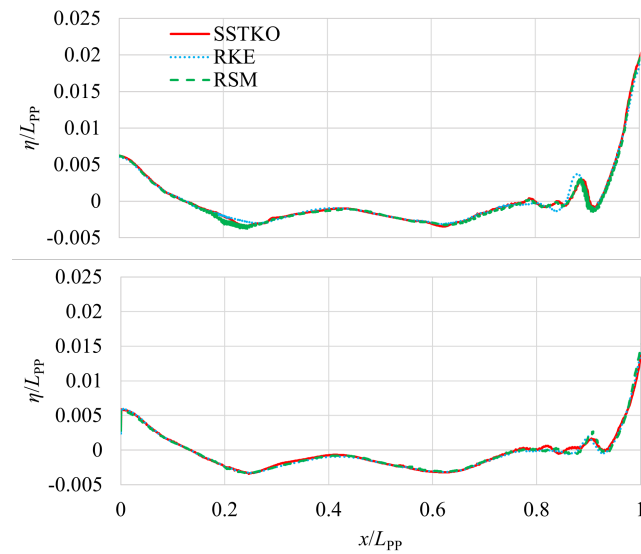


Figure 9. Wave elevations along the hull at full scale (**top**) and model scale (**bottom**) for different turbulence models.

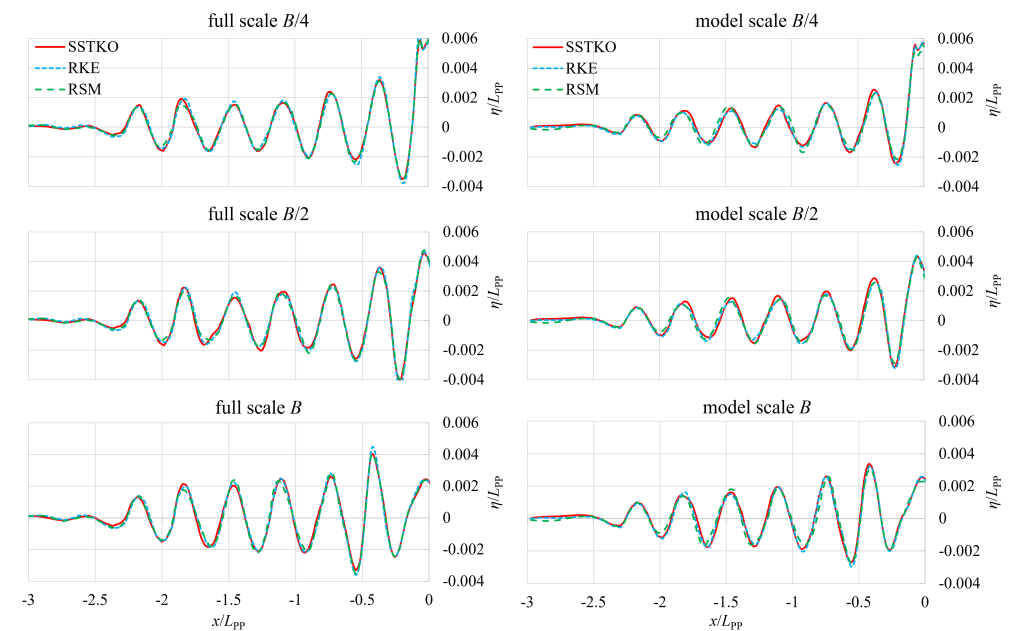


Figure 10. Wave elevations behind the stern at longitudinal cuts $B/4$, $B/2$ and B from the centreline of the ship obtained with numerical simulations at full scale (**left**) and model scale (**right**).

4.3. Discretization Schemes

The impact of the discretization schemes for spatial and temporal discretization is analysed using the fine grid and time step as in the verification study for the full and model scale. The SSTKO turbulence model is used in the remaining numerical simulations. For the cases given in Table 7, the numerical setups are the same at the full and model scales. The STAR-CCM+ default discretization schemes [26] are used in case 1, while remaining cases use different discretization schemes, as shown in Table 7.

Table 7. Different combinations of discretization schemes used in the numerical simulations.

Case	Temporal	Convection	Gradient
1	1st	2nd	2nd
2	1st	1st	2nd
3	1st	3rd	2nd
4	1st	2nd	1st
5	2nd	2nd	2nd
6	1st	1st	1st

4.4. Convection Terms

In this study, the discretization schemes for convection terms are varied within the equations of the turbulence models as well as within the momentum and continuity equations, while maintaining the discretization schemes for gradient and temporal terms as second and first-order, respectively. The considered discretization schemes for convection terms are first-, second- and a hybrid third-order scheme. The third-order scheme is named MUSCL 3rd-order/Central differencing, and it is worth noting that the scheme lowers the order of accuracy in the regions of non-smooth flows.

Figure 11 shows the total resistance values obtained from three numerical simulations at the full scale and three at the model scale. The time range in the graph is displayed from the beginning of the simulations. Using first-order discretization schemes, the total resistance tends to converge considerably faster than in the case with the second-order scheme for the convection terms. Nevertheless, it must be pointed out that the total resistance has higher values for case 2 both at the full and model scale. The amplitudes of the total resistance obtained by second-order discretization scheme are larger and the convergence is much slower than the ones obtained by the first-order scheme. As expected, using the MUSCL 3rd order/Central differencing scheme, the obtained values of total resistance are similar to the ones obtained using second-order scheme. The reason is that this scheme lowers the order of accuracy in the regions of the non-smooth flow.

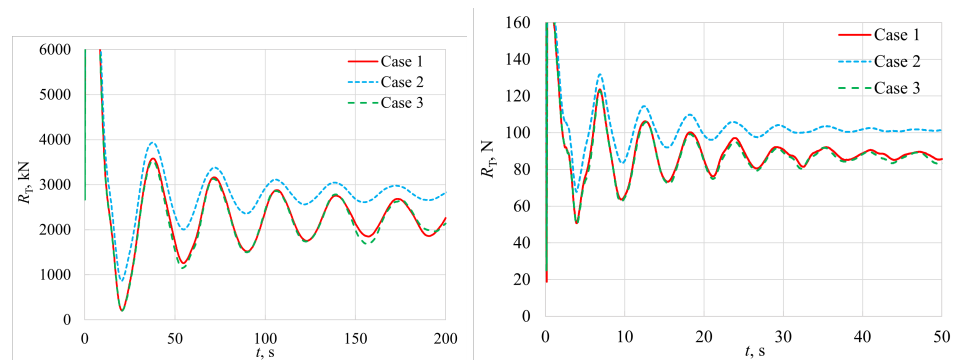


Figure 11. Comparison of three discretization schemes for convection terms at full scale (left) and model scale (right).

Figure 12 shows the values of sinkage and trim as a function of physical time at the full and model scale. The sinkage obtained with numerical simulations at the model scale is scaled with $\lambda = 35.18$ for the comparison with the full-scale results. There are no significant

differences in the obtained sinkage values other than the slightly lower amplitude of the oscillations in the case when first-order scheme is used. On the other hand, the trim values obtained via the first-order scheme for convection terms show a slightly faster convergence at the full scale, while slightly lower amplitudes are obtained at the model scale. The sinkage and trim depend significantly on the scale, with higher sinkage and lower trim values obtained with numerical simulations at the model scale compared to the full scale.

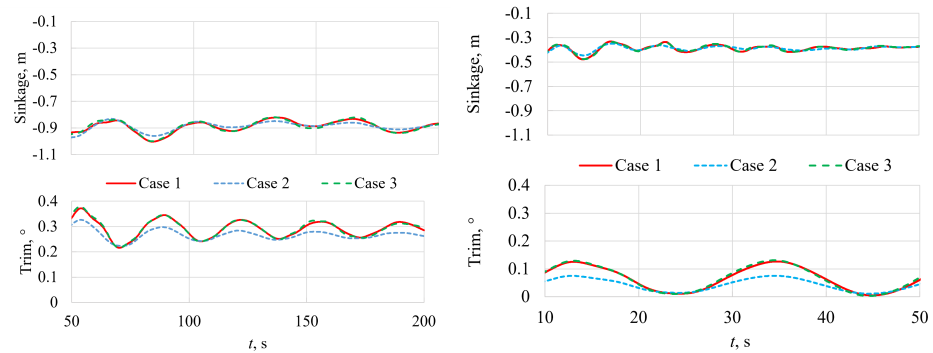


Figure 12. Sinkage and trim values as a function of physical time for different discretization schemes for convection terms at full scale (left) and model scale (right).

Figures 13 and 14 show the wave patterns obtained using the different discretization schemes for convection terms at the full and model scale. The wave elevations obtained with the first-order schemes are noticeably lower in comparison to the ones obtained using higher order schemes. Also, the Kelvin wake is barely visible both at the full and model scale when using the first-order scheme for convection terms. Non-physical perturbations of the free surface outside the Kelvin region can be seen in case 3, where the hybrid third-order discretization scheme for convection terms is used. This effect is slightly less pronounced for the model scale.

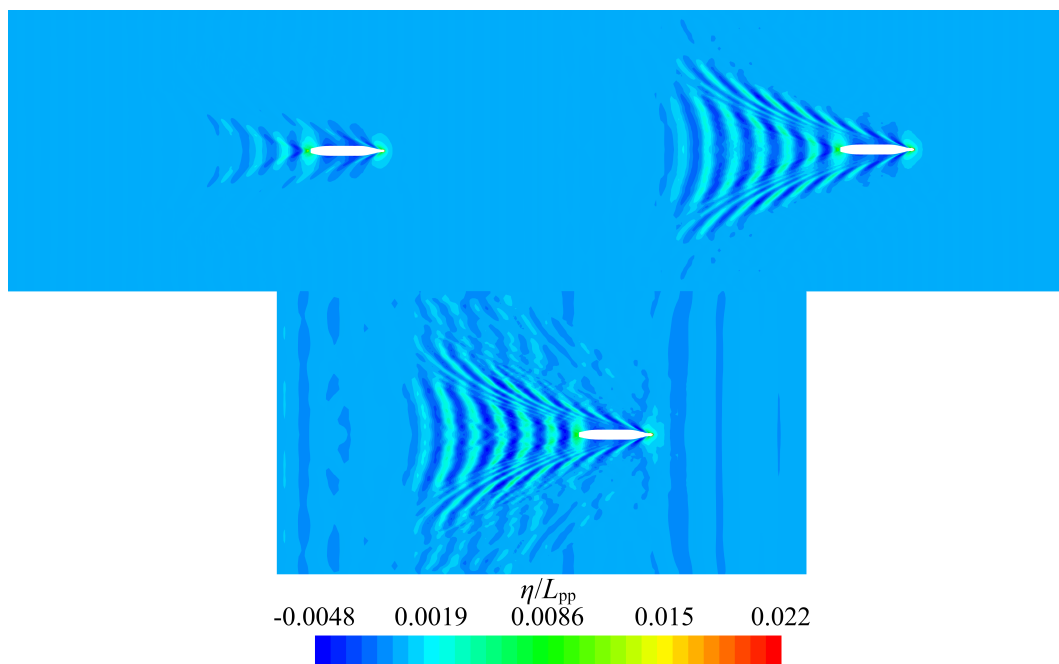


Figure 13. Wave patterns obtained with first-order (top-left), second-order (top-right) and hybrid third-order (bottom) discretization scheme for convection terms at full scale.

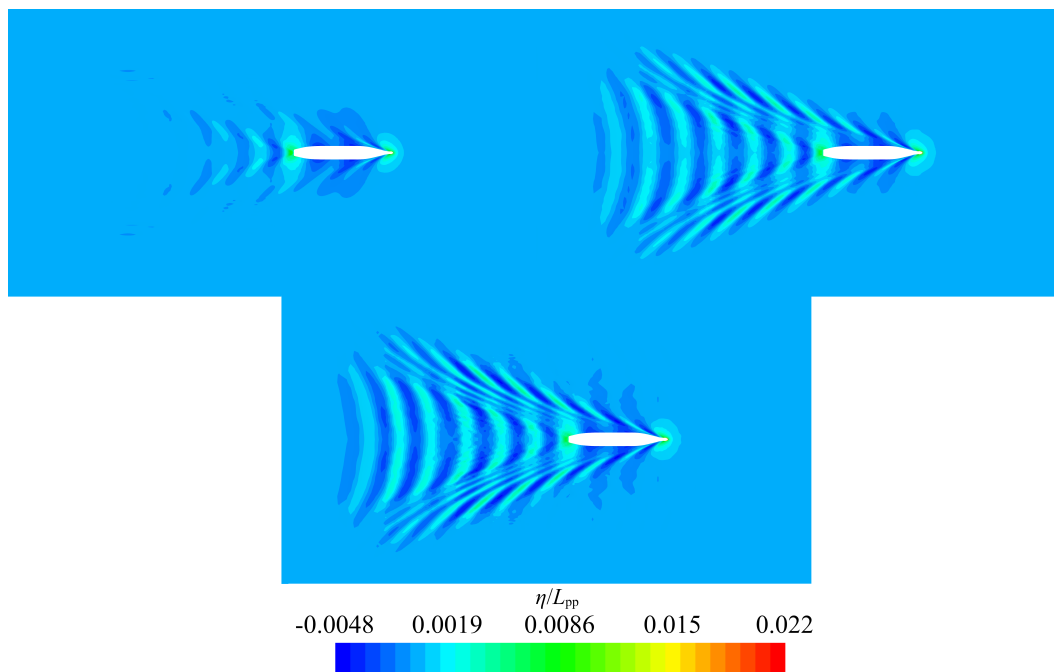


Figure 14. Wave patterns obtained with first-order (**top-left**), second-order (**top-right**) and hybrid third-order (**bottom**) discretization scheme for convection terms at model scale.

Finally, the wave elevations at the centreline of the ship behind the stern and in front of the bow are presented in Figures 15 and 16, respectively, while the wave elevations along the hull are shown in Figure 17. Also, the wave elevations obtained with numerical simulations at the full and model scale behind the stern at longitudinal cuts $B/4$, $B/2$ and B from the centreline of the ship are presented in Figure 18. The results suggest that the choice of the discretization scheme for the convection terms is crucial for the determination of the wave pattern. The wave amplitudes behind the stern decrease significantly faster with first-order scheme in comparison to second and third-order scheme. The same effect can be seen at the full and model scale. The wave elevations along the hull at the model scale are very similar for all three discretization schemes. At the full scale, the first-order scheme yields the lowest elevations, while the hybrid third-order scheme predicts slightly higher elevations.

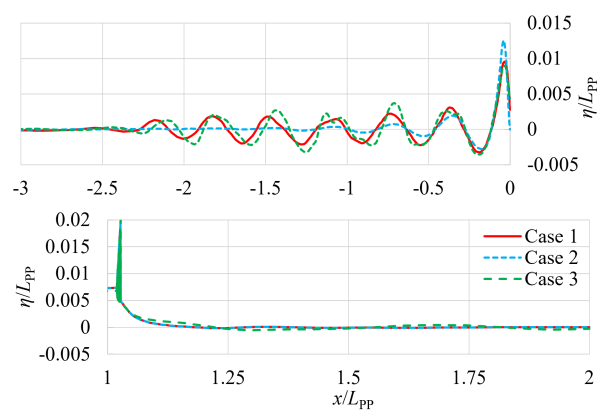


Figure 15. Wave elevations behind the stern (**top**) and in front of the ship (**bottom**), obtained using different discretization schemes for convection terms at full scale.

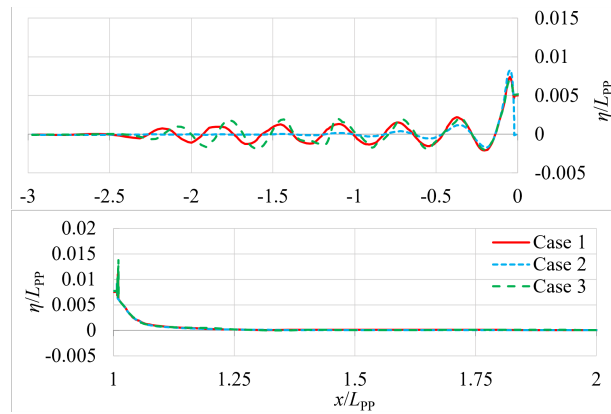


Figure 16. Wave elevations behind the stern (**top**) and in front of the ship (**bottom**), using different discretization schemes for convection terms at model scale.

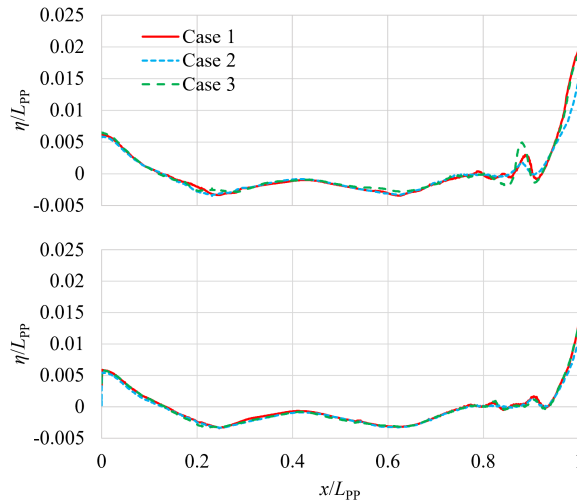


Figure 17. Wave elevations along the hull at full scale (**top**) and model scale (**bottom**) using different discretization schemes for convection terms.

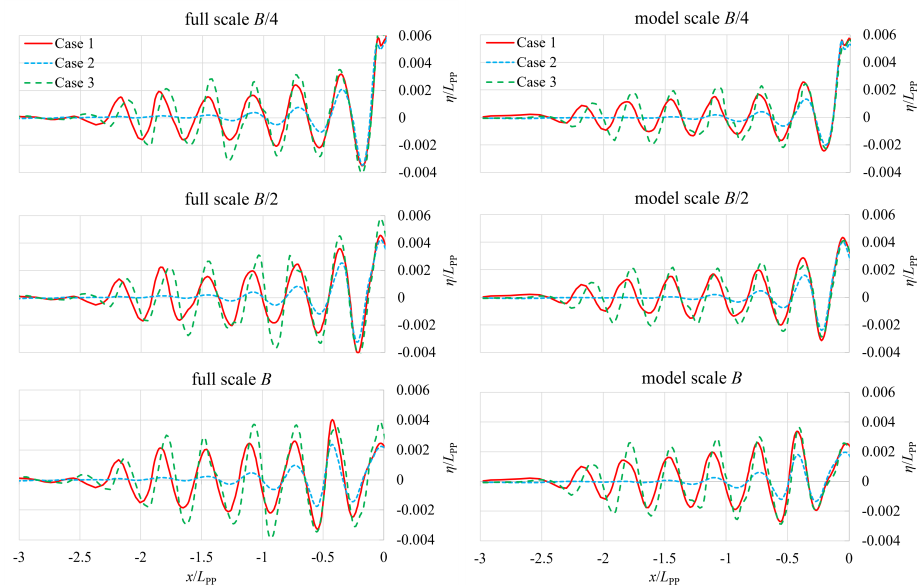


Figure 18. Wave elevations behind the stern at longitudinal cuts $B/4$, $B/2$ and B from the centreline of the ship obtained with numerical simulations at full scale (**left**) and model scale (**right**).

4.5. Gradient Terms

In Section 4.5, the discretization schemes for gradient terms are varied between the first and second order, while the convection terms are kept as second order. The total resistance converges faster with a higher median value using the first-order scheme, as obtained for convection terms in the previous subsection. By comparing Figures 11 and 19, it can be noticed that using the first-order scheme either for gradient or convection terms yields similar results for total resistance. The same is valid for the full and model scale. The main difference between the full and model scale is the faster convergence at the model scale.

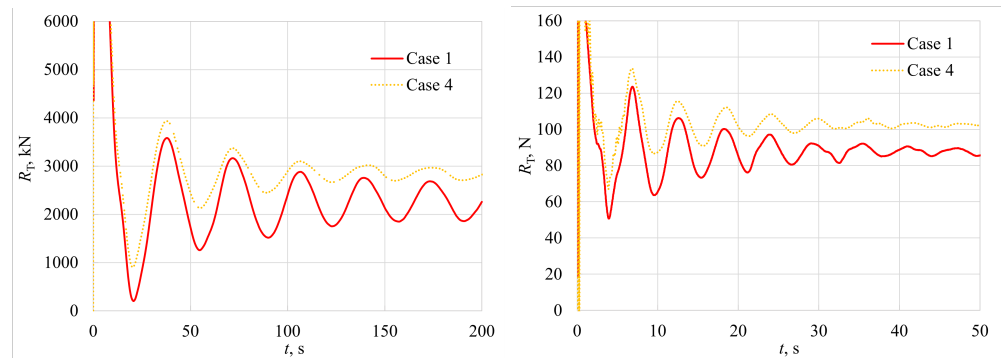


Figure 19. Comparison of two discretization schemes for gradient terms at full scale (left) and model scale (right).

Figures 20 and 21 show a comparison of the wave elevations at the centreline of the ship, obtained using the first- and second-order scheme for gradient terms at the full and model scales. The wave elevations behind the ship obtained using the first-order scheme are significantly lower than the ones obtained using the second-order scheme. The same is obtained in the previous subsection, where the discretization scheme for convection terms is varied. The wave elevations in front of the ship are almost the same in both cases. Figure 22 shows the wave elevations along the hull for different discretization schemes for gradient terms at the full and model scale. Like in the previous analysis of the discretization schemes for convection terms, the first-order scheme for gradient terms yields lower wave elevations along the hull at the full scale. The differences between two discretization schemes at the model scale are negligible in comparison to the full scale.

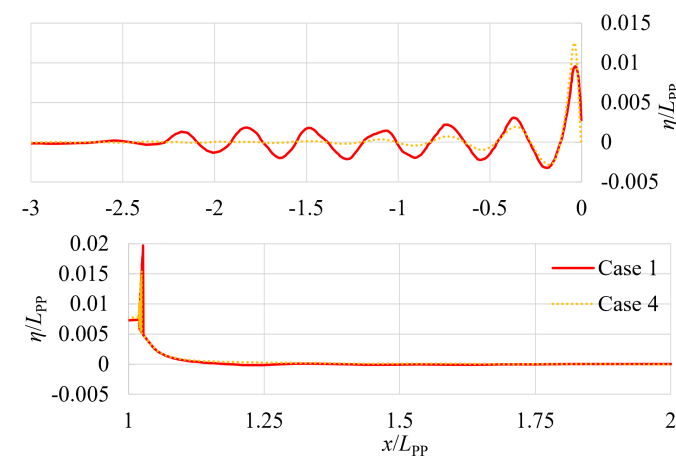


Figure 20. Wave elevations behind the stern (top) and in front of the ship (bottom), obtained using the first and second-order scheme for gradient terms at full scale.

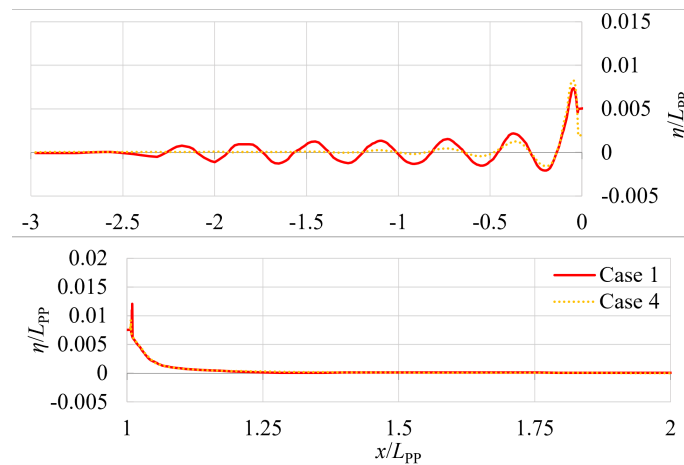


Figure 21. Wave elevations behind the stern (**top**) and in front of the ship (**bottom**), obtained using the first and second-order scheme for gradient terms at model scale.

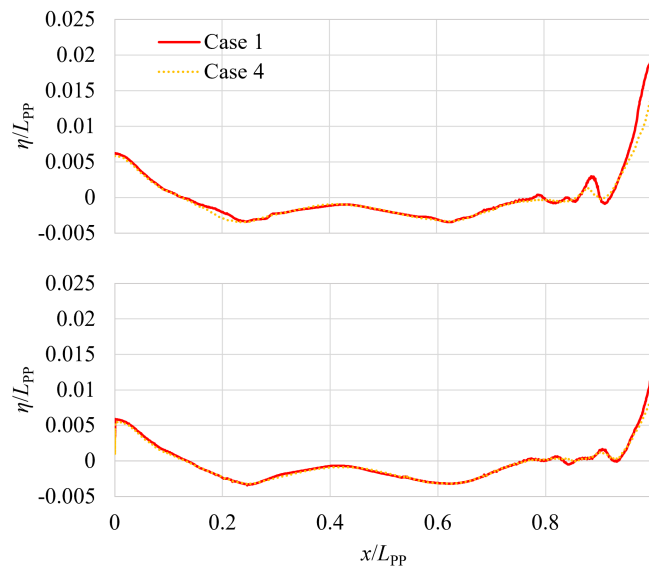


Figure 22. Wave elevations along the hull at full scale (**top**) and model scale (**bottom**) using different discretization scheme for gradient terms.

A comparison between discretization schemes for convection and gradient terms is presented in Figure 23 at the full and model scale in order to assess their impact on numerical results. There are no significant differences between the obtained values of the total resistance at the full and model scale. Thus, it can be concluded that the discretization schemes for solving the convection and gradient terms have a similar impact on the total resistance.

4.6. First-Order vs. Second-Order Schemes

In this Section 4.6, the discretization schemes for all the terms, including temporal discretization, are varied between first and second-order scheme. The details of cases 5 and 6 can be seen in Table 7. The comparison between first- and second-order discretization scheme for gradient, convection and temporal terms is presented in Figure 24 at the full and model scale. A significantly slower convergence of the total resistance is obtained by using the second-order scheme. The oscillations reach higher amplitudes, but with a lower median value. The same is valid for the results obtained using the numerical simulations at the full and model scale, with model scale showing faster convergence using both the first

and second-order discretization scheme, as can be seen from the physical time shown on the abscissa.

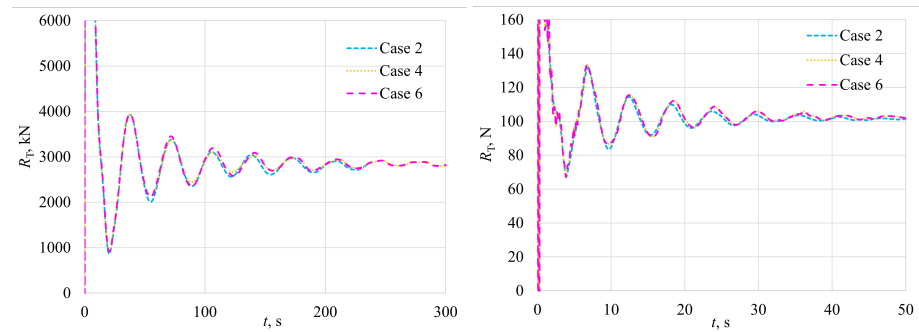


Figure 23. Comparison between first-order scheme for convection and gradient terms at full (left) and model scale (right).

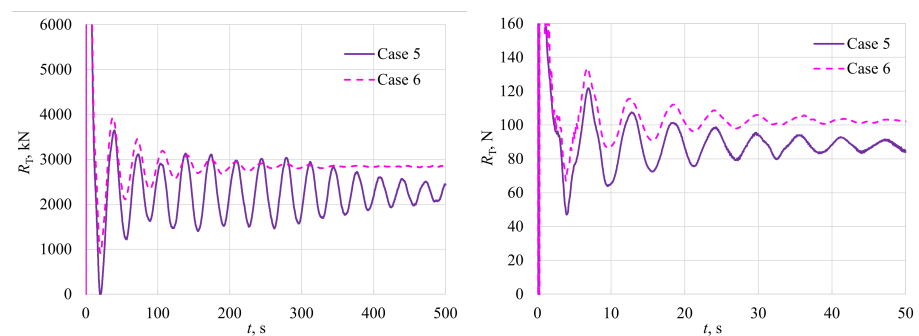


Figure 24. Comparison between first and second-order discretization scheme for gradient, convection terms and temporal discretization at full scale (left) and model scale (right).

Figures 25 and 26 show the obtained wave elevations at the centreline of the ship at full and model scale, respectively. The numerical dissipation, when first-order scheme is applied, is visible at the full and model scale. Figure 27 shows the wave elevations along the ship hull for the full and model scale, obtained using the first and second-order scheme for convection, gradient and temporal terms. Again, lower elevations can be seen at full scale when the first-order scheme is used, while at model scale, the differences are almost negligible. The impact of the discretization scheme for the temporal term on the total resistance at full and model scale is shown in Figure 28. Faster convergence with no significant effect on the median value is obtained with the first-order discretization scheme for the temporal term. At model scale, this effect is negligible in comparison to full-scale results, nevertheless, it is still visible.

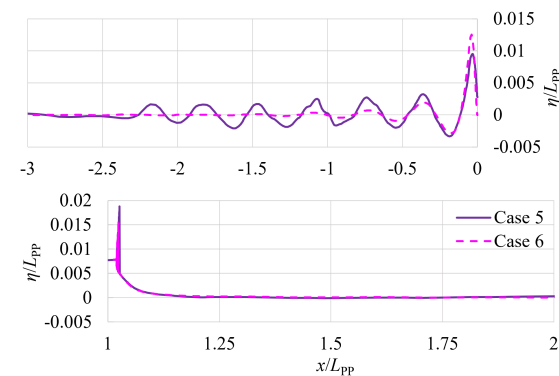


Figure 25. Wave elevations behind the stern (top) and in front of the ship (bottom), obtained using different discretization schemes for spatial and temporal terms at full scale.

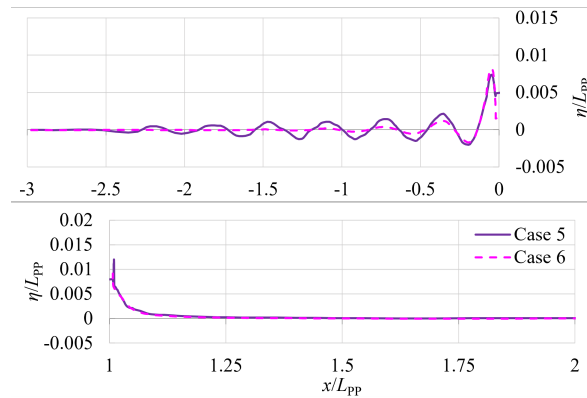


Figure 26. Wave elevations behind the stern (**top**) and in front of the ship (**bottom**), obtained using different discretization schemes for spatial and temporal terms at model scale.

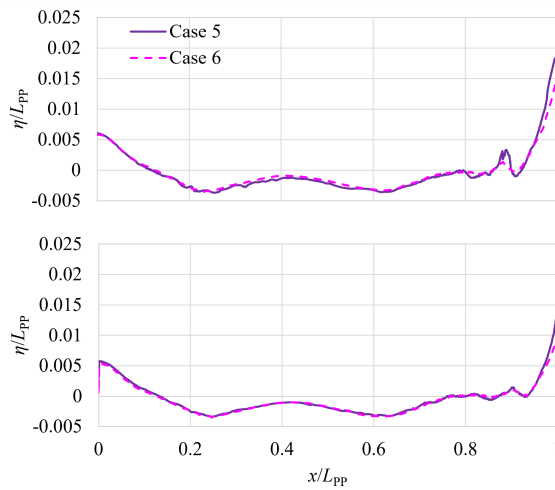


Figure 27. Wave elevations along the hull at full scale (**top**) and model scale (**bottom**) using different discretization schemes for spatial and temporal terms.

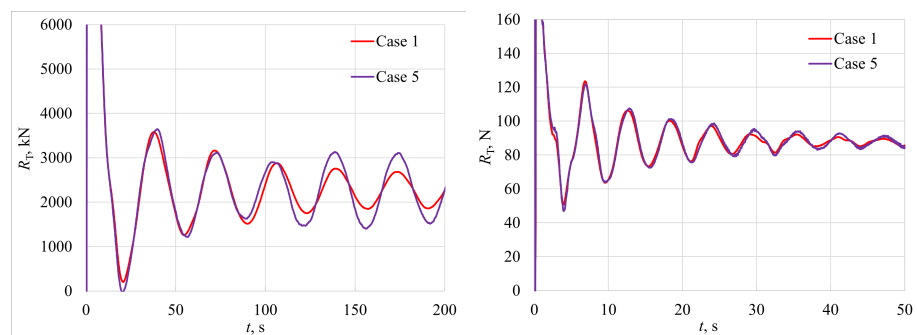


Figure 28. The impact of the temporal discretization on the total resistance at full scale (**left**) and model scale (**right**).

Figure 29 shows the wave elevations behind the stern at longitudinal cuts $B/4$, $B/2$ and B from the centreline of the ship obtained with numerical simulations at the full and model scale. The wave elevations obtained from numerical simulations at the full scale are higher for case 5 in comparison to case 1. On the contrary, at the model scale, the wave elevations behind the ship for case 5 are lower in comparison to case 1. As expected, lower elevations can be seen at sections further away from the centreline of the ship for the full and model scales.

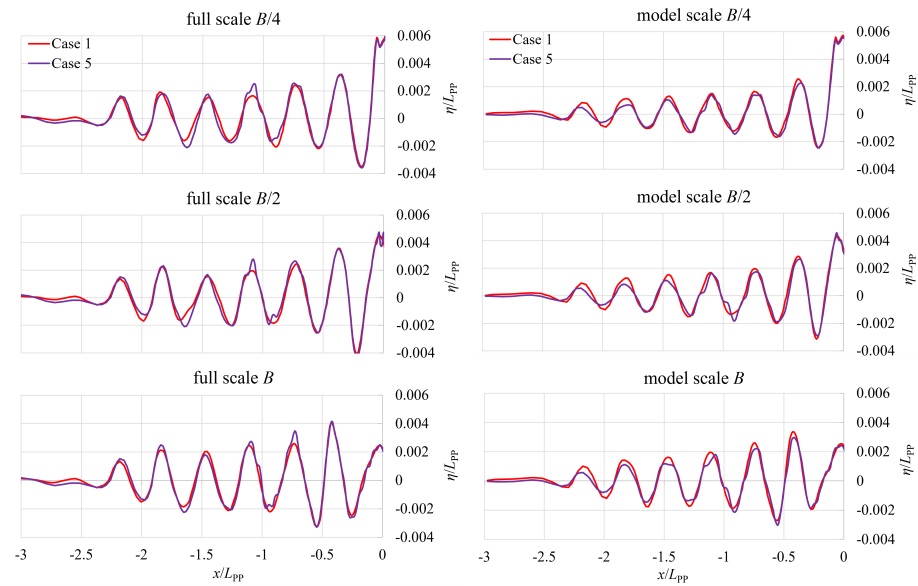


Figure 29. Wave elevations behind the ship at longitudinal cuts $B/4$, $B/2$ and B from the centreline of the ship obtained with numerical simulations at full scale (left) and model scale (right).

4.7. Resistance Components

In Section 4.7, the total resistance obtained within the free surface simulations is decomposed into the frictional R_F and pressure R_P resistance. These components are obtained by integrating the tangential stress and pressure, obtained with free surface simulations, over the wetted surface, respectively. The results obtained with numerical simulations at the full and model scale are shown in Figures 30 and 31 for the cases listed in Table 7. The frictional resistance is almost the same for all the cases at the full and model scales. The pressure resistance changes with the different discretization schemes more significantly in comparison to the frictional resistance. Also, the portion of the frictional resistance in the total resistance is significantly higher at the model scale, with a median value of 76.2%, than at the full scale, where its portion is 59.5%. It can be concluded that the portion of the frictional resistance decreases, while the portion of the pressure resistance becomes more significant at the full scale in comparison to the model scale.

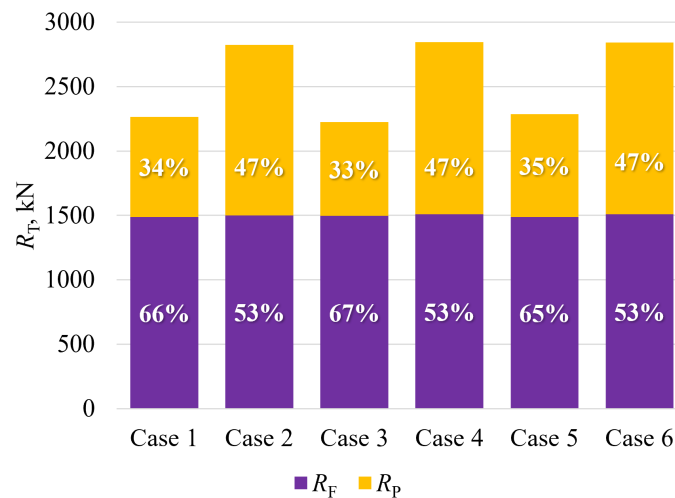


Figure 30. The portions of the total resistance components obtained with numerical simulations at full scale.

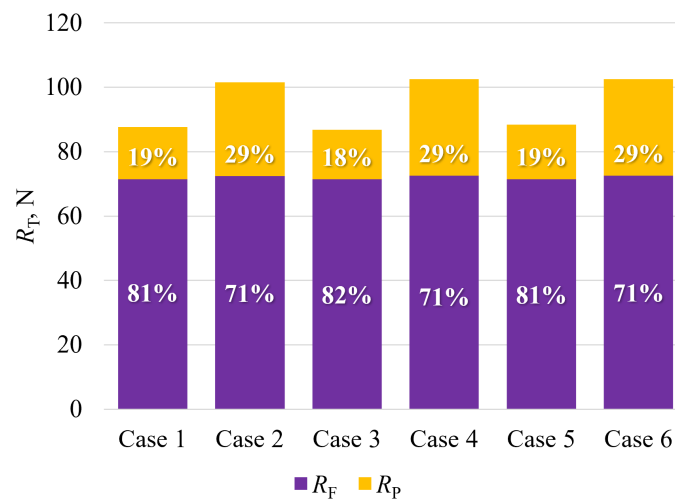


Figure 31. The portions of the total resistance components obtained with numerical simulations at model scale.

Figure 32 shows the portions of the total resistance components obtained with three turbulence models within the numerical simulations at the full and model scale. Similarly to the results of the previous analysis, the median value of the portion of the frictional resistance in the total resistance at the model scale is 82%, which is noticeably higher than that at the full scale, where the median value of the portion of the frictional resistance is 66.7%. The portions of the total resistance components do not change significantly with different turbulence models, even though the total resistance does change.

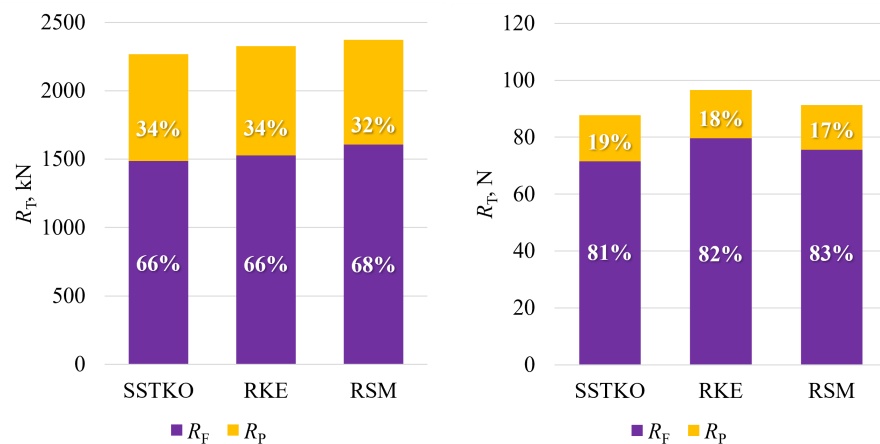


Figure 32. The portions of the total resistance components obtained with different turbulence models within the numerical simulations at full scale (left) and model scale (right).

5. Conclusions

Numerical simulations of the flow around the model- and full-scale post-Panamax container ship were performed, and the numerical setup was described in detail along with the overview of the meshing process. The grid was refined in the region of the Kelvin wake, the approximate location of the free surface and the boundary layer around the ship hull. In order to apply wall functions, the boundary layer was discretized to maintain the non-dimensional wall distance y^+ in the range $30 < y^+ < 100$. The numerical uncertainty was calculated using the Grid Convergence Index (GCI) method for the grid size and time step. The monotonic convergence of the results was obtained for three grid sizes and three time steps at the full scale, while oscillatory convergence was obtained for numerical simulations at the model scale. A validation study was conducted using the

numerical results obtained with three turbulence models and experimental results from the towing tank. After the verification and validation studies were completed, the impact of different numerical parameters on the total resistance, wave pattern and ship motion was analysed. These included turbulence models and the discretization schemes for the convection, gradient and temporal terms. The considered turbulence models included the Realizable $k - \epsilon$ (RKE), Shear Stress Transport $k - \omega$ (SSTKO) and Reynolds Stress (RSM). The results have shown that the total resistance obtained using the SSTKO turbulence model at the full scale differs from the ones obtained using RKE and RSM. A similar trend was noticed for numerical simulations at the model scale, where the SSTKO turbulence model yielded lower values of the total resistance in comparison to RKE turbulence model. Also, the total resistance obtained by the RSM turbulence model differs with scale. The total resistance obtained by RSM turbulence model at the full scale is almost the same as the one obtained with RKE, while at the model scale, the values are closer to the ones obtained by SSTKO turbulence model. Slightly lower sinkage values are obtained using the RSM model for the model and full scale, while the trim does not depend on the chosen turbulence model.

For the convection terms, the first-, second- and hybrid third-order discretization schemes were analysed. Faster convergence of the total resistance was obtained when the first-order scheme was applied, but the total resistance was higher than that with the second- and hybrid third-order scheme. Also, the wave pattern obtained with the first-order scheme had lower amplitudes and dissipated faster behind the ship in comparison to the other two schemes. The wave pattern obtained by the hybrid third-order scheme showed some unphysical perturbations in the region outside the Kelvin wake. This effect was slightly less visible at the model scale. Similarly, the impact of the discretization scheme for solving the gradient terms on the numerical results was assessed. The gradient terms in this analysis are solved using the first and second-order discretization scheme. Similar results are obtained as in the analysis of the convection terms. Higher total resistance was obtained with faster convergence when the first-order scheme was applied. The wave elevations at the centreline of the ship had lower amplitudes behind the stern. After the discretization schemes for convection and gradient terms were analysed separately, their impact on the obtained numerical results together with the discretization scheme for temporal terms was assessed. Compared to the second-order scheme, faster convergence with a higher median value of total resistance was obtained with the first-order scheme. Finally, the impact of the discretization scheme for temporal term was assessed. It has been shown that the selection of the discretization scheme for solving the temporal term does not impact the median value of the total resistance and that the first-order scheme assures faster convergence in numerical simulations at the full scale. In numerical simulations at the model scale, the first-order scheme speeds up the convergence of the total resistance as well, but at a slower rate.

Finally, the total resistance was decomposed into frictional and pressure resistance. It has been shown that the frictional resistance does not depend significantly on the discretization scheme for the convection, gradient and temporal terms. On the other hand, the discretization schemes for convection and gradient terms affect the pressure resistance, which is higher when the first-order scheme is used. The total resistance changes with the chosen turbulence model, but the portions of frictional and pressure resistance remain nearly the same. Also, both analyses showed that a higher portion of frictional resistance within the total resistance is obtained with numerical simulations at the model scale in comparison to the full scale.

Author Contributions: Conceptualization, C.G.G., N.D. and I.M.; methodology, C.G.G., N.D. and I.M.; software, C.G.G.; validation, C.G.G., N.D. and I.M.; formal analysis, C.G.G., N.D. and I.M.; investigation, C.G.G., N.D. and I.M.; resources, N.D.; writing—original draft preparation, C.G.G., N.D. and I.M.; writing—review and editing, C.G.G., N.D. and I.M.; visualization, C.G.G.; supervision, N.D.; project administration, C.G.G., N.D. and I.M. All authors have read and agreed to the published version of the manuscript.

Funding: This study was funded by the Croatian Science Foundation under project IP-2020-02-8568.

Institutional Review Board Statement: Not applicable.

Informed Consent Statement: Not applicable.

Data Availability Statement: Not applicable.

Acknowledgments: This study has been fully supported by the Croatian Science Foundation under project IP-2020-02-8568.

Conflicts of Interest: The authors declare no conflicts of interest.

References

1. Terziev, M.; Tezdogan, T.; Demirel, Y.K.; Villa, D.; Mizzi, S.; Incecik, A. Exploring the effects of speed and scale on a ship's form factor using CFD. *Int. J. Nav. Arch. Ocean* **2021**, *13*, 147–162.
2. Orych, M.; Werner, S.; Larsson, L. Validation of full-scale delivered power CFD simulations. *Ocean Eng.* **2021**, *238*, 109654.
3. Saydam, A.Z.; Küçüküsu, G.N.; Insel, M.; Gökçay, S. Uncertainty quantification of self-propulsion analyses with RANS-CFD and comparison with full-scale ship trials. *Brodogradnja* **2022**, *73*, 107–129.
4. Degiuli, N.; Martić, I.; Farkas, A.; Gospić, I. The impact of slow steaming on reducing CO₂ emissions in the Mediterranean Sea. *Energy Rep.* **2021**, *7*, 8131–8141.
5. Demirel, Y.K.; Turan, O.; Incecik, A. Predicting the effect of biofouling on ship resistance using CFD. *Appl. Ocean Res.* **2017**, *62*, 100–118.
6. Song, S.; Demirel, Y.K.; Muscat-Fenech, C.D.M.; Tezdogan, T.; Atlar, M. Fouling effect on the resistance of different ship types. *Ocean Eng.* **2020**, *216*, 107736.
7. Feng, D.; Ye, B.; Zhang, Z.; Wang, X. Numerical Simulation of the Ship Resistance of KCS in Different Water Depths for Model-Scale and Full-Scale. *J. Mar. Sci. Eng.* **2020**, *8*, 745.
8. Niklas, K.; Pruszek, H. Full-scale CFD simulations for the determination of ship resistance as a rational, alternative method to towing tank experiments. *Ocean Eng.* **2019**, *190*, 106435.
9. Dogrul, A. Numerical Prediction of Scale Effects on the Propulsion Performance of Joubert BB2 Submarine. *Brodogradnja* **2022**, *73*, 17–42.
10. Song, K.; Guo, C.; Sun, C.; Wang, C.; Gong, J.; Li, P.; Wang, L. Simulation strategy of the full-scale ship resistance and propulsion performance. *Eng. Appl. Comp. Fluid* **2021**, *15*, 1321–1342.
11. Andrun, M.; Blagojević, B.; Bašić, J. The influence of numerical parameters in the finite-volume method on the Wigley hull resistance. *Proc. Inst. Mech. Eng. M-J. Eng.* **2019**, *233*, 1123–1132. [CrossRef]
12. Huang, L.; Pena, B.; Thomas, G. Towards a full-scale CFD guideline for simulating a ship advancing in open water. *Ship Technol. Res.* **2023**, 1–17. [CrossRef]
13. Farkas, A.; Degiuli, N.; Martić, I. Assessment of hydrodynamic characteristics of a full-scale ship at different draughts. *Ocean Eng.* **2018**, *156*, 135–152. [CrossRef]
14. Degiuli, N.; Farkas, A.; Martić, I.; Zeman, I.; Ruggiero, V.; Vasiljević, V. Numerical and experimental assessment of the total resistance of a yacht. *Brodogradnja* **2021**, *72*, 61–80. [CrossRef]
15. Kim, Y.; Kim, J.H. Benchmark study on motions and loads of a 6750-TEU containership. *Ocean Eng.* **2016**, *119*, 262–273. [CrossRef]
16. Brodarski Institute. *Report 6655-M. Resistance, Self-Propulsion and 3D Wake Measurement Test Results*; Brodarski Institute: Zagreb, Croatia, 2022.
17. Siemens. STAR-CCM+ User Guide. 2020. Available online: <https://www.cfd-online.com/Forums/star-ccm/240557-star-ccm-user-guide-tutorials.html> (accessed on 19 July 2023).
18. Menter, F.R. Two-equation eddy-viscosity turbulence models for engineering applications. *AIAA J.* **1994**, *32*, 1598–1605. [CrossRef]
19. ITTC. Practical Guidelines for Ship CFD Applications, 7.5-03-02-03. In *ITTC-Recommended Procedures and Guidelines*; ITTC: Rio de Janeiro, Brazil, 2011.
20. Grlj, C.G.; Degiuli, N.; Farkas, A.; Martić, I. Numerical Study of Scale Effects on Open Water Propeller Performance. *J. Mar. Sci. Eng.* **2022**, *10*, 1132. [CrossRef]
21. Celik, I.B.; Ghia, U.; Roache, P.J.; Freitas, C.J.; Coleman, H.; Raad, P.E. Procedure for estimation and reporting of uncertainty due to discretization in CFD applications. *J. Fluids Eng.* **2008**, *130*, 0780011–0780014.
22. Song, S.; Demirel, Y.K.; Atlar, M.; Dai, S.; Day, S.; Turan, O. Validation of the CFD approach for modelling roughness effect on ship resistance. *Ocean Eng.* **2020**, *200*, 107029. [CrossRef]
23. Mikkelsen, H.; Walther, J.H. Effect of roughness in full-scale validation of a CFD model of self-propelled ships. *Appl. Ocean Res.* **2020**, *99*, 102162. [CrossRef]
24. Kahramanoglu, E.; Yıldız, B.; Çakıcı, F.; Yilmaz, H. Numerical roll damping prediction of a planing hull. *Ship Offshore Struct.* **2021**, *16*, 363–372. [CrossRef]

25. Pena, B.; Huang, L. A review on the turbulence modelling strategy for ship hydrodynamic simulations. *Ocean Eng.* **2021**, *241*, 110082. [[CrossRef](#)]
26. Mikulec, M.; Piehl, H. Verification and validation of CFD simulations with full-scale ship speed/power trial data. *Brodogradnja* **2023**, *74*, 41–62. [[CrossRef](#)]

Disclaimer/Publisher's Note: The statements, opinions and data contained in all publications are solely those of the individual author(s) and contributor(s) and not of MDPI and/or the editor(s). MDPI and/or the editor(s) disclaim responsibility for any injury to people or property resulting from any ideas, methods, instructions or products referred to in the content.